

Cite this: *Chem. Sci.*, 2018, 9, 3341

# A first-principles prediction on the “healing effect” of graphene preventing carrier trapping near the surface of metal halide perovskites†

W.-W. Wang,<sup>ab</sup> J.-S. Dang,<sup>ab</sup> R. Jono,<sup>a</sup> H. Segawa<sup>\*a</sup> and M. Sugimoto<sup>id\*ab</sup>

We herein report that surface modification of metal halide perovskites using graphene would be beneficial to improving the energy conversion efficiencies of perovskite solar cells. The present first-principles calculations on MAPbI<sub>3</sub> with a single vacancy created by removing either I, Pb or MA show that the I and Pb vacancies near the surface result in the formation of Pb–Pb and I–I dimers, respectively. They are predicted to yield mid-gap levels, and would degrade the energy conversion efficiency of perovskite solar cells through carrier trapping. The present calculations suggest that when the surface of MAPbI<sub>3</sub> is covered with a graphene sheet, the formation of the carrier trapping dimers would be suppressed. The origin of the “healing effect” of graphene on the lattice defect is ascribed to electronic interactions on the surface, which prevent charge localization at the lattice defects beneath the surface.

Received 9th November 2017  
Accepted 22nd February 2018

DOI: 10.1039/c7sc04837h

rsc.li/chemical-science

## 1 Introduction

Metal halide perovskites (e.g. methylammonium lead iodide (MAPbI<sub>3</sub>)) have been proved to be promising materials for photovoltaic applications because of their feasible and tunable band gaps,<sup>1</sup> high and balanced charge-carrier mobilities,<sup>2</sup> and long electron–hole diffusion lengths.<sup>3</sup> In particular, the power conversion efficiency (PCE) of perovskite solar cells (PSCs) has dramatically increased from 3.8% in 2009 to a recently certified 22.1%.<sup>4,5</sup> Despite the impressive development, current efficiencies of PSCs are still far from the theoretical maximum of 30–33%.<sup>6,7</sup> One important issue is the effect of perovskite defects which is strongly related to the electrical instability and formation of charge trapping states.<sup>7</sup> In particular, the defect-mediated interfacial carrier (hole and electron) recombination process is considered as an important loss mechanism of perovskite solar cells.<sup>8</sup> Previous studies have proposed that defects or impurities of perovskite thin films prefer to be concentrated at the grain boundaries and interface between the perovskite and the neighbouring charge transporting layers,<sup>9–13</sup> which assist non-radiative carrier recombination and significantly affect the short-circuit current and open-circuit voltage of devices.

To avoid the defect-induced interfacial traps, careful control of the perovskite crystallinity and interface optimization *via*

incorporation of additional materials are two feasible strategies in practice.<sup>14–22</sup> Among the limited studies that made efforts to understand the role of surface defects and detrapping mechanisms,<sup>7,16,17,23,24</sup> the incorporation of PCBM ([6,6]-phenyl-C<sub>61</sub>-butyric acid methyl ester) was reported as a unique way to reduce trap states caused by Pb–I antisite defects.<sup>16,17</sup> Experimental evidence indicated that PCBM distributes around the perovskite surface and passivates the antisite defects *via* electron transfer with anionic iodines.<sup>17</sup> As a result the recombination and current–voltage (*J*–*V*) hysteresis are suppressed and the device performance is correspondingly improved.

Besides fullerene and its derivatives, graphene is another promising sp<sup>2</sup> nano-carbon material which has been widely used in PSCs as an interlayer to achieve improved contact between the perovskite and the neighbouring charge transporting layers, better charge transport characteristics, and enhanced device stabilities.<sup>25–34</sup> However, to date, there have been hardly any investigations on the role of graphene in interface modification and the relationship between graphene and surface defects of perovskites. Of particular interest is the understanding of defective vacancies at the surface in the presence of graphene. Compared to other types of point defects, single vacancies of MAPbI<sub>3</sub> perovskites, including iodine vacancies, lead vacancies, and MA vacancies, are considered as a major type of structural defects because of their relatively low formation energies.<sup>7,8,35</sup> So far most studies on perovskite vacancies have mainly focused on intrinsic defects which are believed to not form deep-level defects for carrier trapping.<sup>8,35–44</sup> In contrast, systematic investigations on defective perovskites with surface vacancies are still limited.<sup>45,46</sup> Therefore it is of great interest to explore the nature of vacancy defects around the perovskite surface as well as the role of graphene on the surface.

<sup>a</sup>Research Center for Advanced Science and Technology, The University of Tokyo, 4-6-1 Komaba, Meguro-ku, Tokyo 153-8904, Japan. E-mail: csegawa@mail.ecc.u-tokyo.ac.jp

<sup>b</sup>Faculty of Advanced Science and Technology, Kumamoto University, 2-39-1 Kurokami, Chuo-ku, Kumamoto 860-8555, Japan. E-mail: sugimoto@kumamoto-u.ac.jp

† Electronic supplementary information (ESI) available: Detailed information on the geometries, energies, charge distributions, and density of states of relevant structures. See DOI: 10.1039/c7sc04837h

In the present work, first-principles calculations were carried out to study the properties of defective perovskite MAPbI<sub>3</sub> with single vacancies. The results showed that the I or Pb vacancies around the surface region are prone to generate deep-level defects by producing Pb–Pb or I–I dimers, respectively. What is more important is that the incorporation of a graphene layer on the top of the perovskite gives rise to the modification of defective sites and the trap states are effectively eliminated, which can be attributed to the interfacial charge transfer between graphene and surface Pb or I atoms. In addition, this healing effect by the incorporation of an interlayer was extended to the use of small organic molecules. The results showed that surface passivation by employing electron-deficient hydrocarbons (*e.g.* ethylene and benzene) or molecules with a lone pair (*e.g.* pyridine) can also eliminate the trap states induced by surface vacancies.

## 2. Computational methods

First-principles calculations were performed using density functional theory in the CASTEP code.<sup>47,48</sup> The Perdew–Burke–Ernzerhof (PBE) generalized gradient approximation was used to describe the exchange–correlation interactions.<sup>49</sup> Tkatchenko–Scheffler (TS) custom DFT-D parameters were adopted to describe the empirical dispersion correction.<sup>50</sup> The ionic cores and core–valence interactions were described using the ultra-soft pseudopotentials, and the kinetic energy cutoff was set to 500 eV.<sup>51</sup>

The tetragonal MAPbI<sub>3</sub> ( $\beta$ -phase) was used as the perovskite material. In this work we investigated all three types of single vacancies of MAPbI<sub>3</sub>, *i.e.* iodine vacancy ( $V_I$ ), lead vacancy ( $V_{Pb}$ ), and MA vacancy ( $V_{MA}$ ). Both the supercell and slab models were employed to explore the influence of vacancies in different positions (bulk or surface region of crystals). Note that the defective structures with single vacancies are studied in neutral states. The bulk tetragonal-MAPbI<sub>3</sub> was optimized using a  $2\sqrt{2} \times 2\sqrt{2} \times 4$  supercell containing 32 formula units ( $17.600 \times 17.600 \times 25.370 \text{ \AA}^3$ ), as shown in Fig. 1. For slab calculations, discussions in the present work were mainly focused on a  $2 \times 2 \times 3.5$  tetragonal-MAPbI<sub>3</sub> model (Slab1, see Fig. 1) with a (110)-surface which was determined to be one of the most predominant MAPbI<sub>3</sub> facets in experiments,<sup>52</sup> with a calculated band gap of 1.352 eV (Table S1 of the ESI†). Moreover, the constructed slab model is terminated by a PbI<sub>2</sub> layer rather than a MAI layer because our calculations based on two smaller  $2 \times 2 \times 2.5$  MAPbI<sub>3</sub> slabs (labelled Slab2 and Slab3 in Fig. S1 of the ESI†) show that the binding energy ( $E_b$ ) of the PbI<sub>2</sub>–graphene interface is 0.41 eV larger than that of the MAI–graphene interface (see Table S2 and Fig. S2 of the ESI†). In addition, to check the influence of slab size on the results, calculations were repeated by using a larger  $4 \times 2 \times 2.5$  structure (Slab4 in Fig. S1 of the ESI†). The results (Fig. S3 of the ESI†) showed that similar properties can be obtained by using different slab models, indicating that the slabs we used are large enough to get reliable outcomes. Note that the Brillouin zone was described using  $1 \times 1 \times 1$  for the bulk model and  $2 \times$



Fig. 1 (a) Bulk and (b) slab MAPbI<sub>3</sub> models adopted in the present study.

$2 \times 1$  (Slab1)/ $4 \times 4 \times 1$  (Slab2 and Slab3)/ $1 \times 2 \times 1$  (Slab4) grids for different slab structures. As for the graphene incorporated hybrid structures, experimental lattice constants of MAPbI<sub>3</sub> were adopted (with an average Pb–Pb distance of 6.263 Å) during geometry relaxations,<sup>53</sup> and the lattice mismatch between MAPbI<sub>3</sub> and graphene was 1% only. It is worth noting that a vacuum region of more than 25 Å was used for each slab model, in order to avoid interactions between periodic images. The atomic positions were fully relaxed for the optimization of each slab model in the present work.

## 3 Results and discussion

### 3.1. MAPbI<sub>3</sub> with an I vacancy

First, we focused on the defective perovskites with a single iodine vacancy ( $V_I$ ). For a bulk tetragonal-MAPbI<sub>3</sub> model with this point defect, geometry optimization showed that structural relaxation around the  $V_I$  is small and the bulk structure is maintained. This is reflected in the Pb–Pb distance near the  $V_I$ . It was calculated to be 6.278 Å (Fig. S4 of the ESI†), which is comparable to that in the bulk (6.263 Å). The calculated density of states (DOS) (see Fig. S5 of the ESI†) reveals that the  $V_I$  in the bulk gives rise to a shallow-level defect below the conduction band edge. Since the  $V_I$  is formed by removing a neutral I atom in the present modelling, this shallow level is occupied by an electron. Thus, this defective system exhibits an n-type character. These features of the bulk defect are essentially similar to those reported by Zhang *et al.*<sup>8</sup>

In order to investigate the surface of MAPbI<sub>3</sub> with a  $V_I$ , we employed four types of 3.5-layered tetragonal-MAPbI<sub>3</sub> slab models with a single  $V_I$  labelled Slab1\_ $V_I$ -1, -2, -3, and -4, given in Fig. 2. In these models, the position of the  $V_I$  is different. The  $V_I$  resides around the surface region in Slab1\_ $V_I$ -1 (on the PbI<sub>2</sub> layer) and Slab1\_ $V_I$ -2 (on the MAI layer), whereas it locates at intrinsic positions in cases of Slab1\_ $V_I$ -3 (on the PbI<sub>2</sub> layer) and



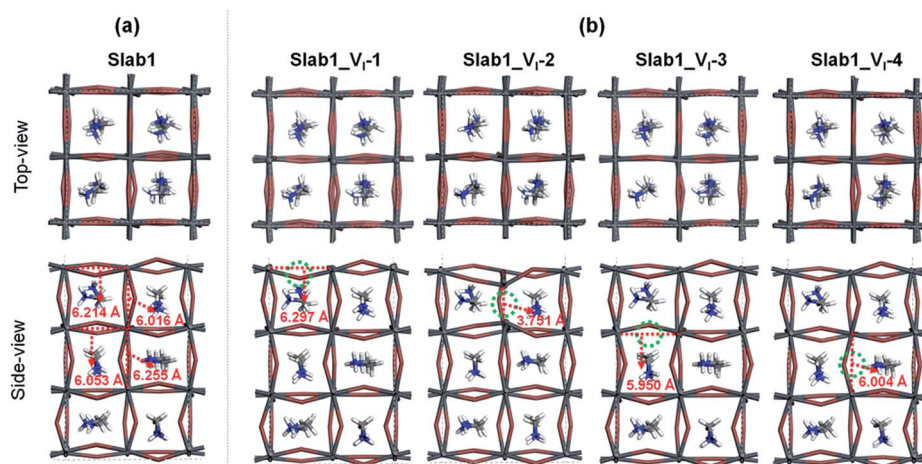


Fig. 2 (a) Defect-free and (b)  $V_I$ -containing defective  $\text{MAPbI}_3$  slabs. The dashed circles indicate the position of the  $V_I$ . Each number in (b) indicates the Pb–Pb distance around the  $V_I$ .

Slab1\_ $V_I$ -4 (on the MAI layer). As mentioned above, compared to the well-studied intrinsic vacancies in bulk, the characteristics of surface and interfacial vacancies of perovskites are still rarely known. For comparison, the perfect (defect-free) slab model was also optimized by using DFT calculations.

Among the optimized structural parameters, we find a notable change in Slab1\_ $V_I$ -2 (Fig. 2(b)): the Pb–Pb distance around the  $V_I$ , which is perpendicular to the (110)-surface ( $a, b$ -plane), is greatly shortened to 3.751 Å. This is in sharp contrast to the corresponding Pb–Pb distance (6.016 Å) in the defect-free slab model. In Slab1\_ $V_I$ -1, -3, and -4, the Pb–Pb distances near the  $V_I$  are 6.297, 5.950, and 6.004 Å, respectively. These values are close to those in the defect-free slab and aforementioned bulk models with a  $V_I$ .

The features of the geometry changes are well reflected in the density of states (DOS) of the Slab1\_ $V_I$  models where the Fermi level (the highest occupied level) is set to 0 eV. The Fermi level in the defect-free slab model is located at the top of the valence band as shown in Fig. 3. The band gap of this model is 1.352 eV, which is comparable to the experimental value of 1.52 eV.<sup>54</sup> Fig. 4(a) shows the DOS of the defective slab model of Slab1\_ $V_I$  before geometry optimization. These data indicate that when

a neutral I atom is removed, the Fermi level is located at the conduction band edge. The DOSs of the conduction band of the defective systems are essentially similar. This is also true except that the valence band onset of Slab\_ $V_I$ -1 is slightly shifted to low energy.

After geometry optimization, the DOS of Slab\_ $V_I$ -2 becomes different from those of the other three systems as shown in Fig. 4(b). In the former, the conduction band bottom splits into two moieties, and the low-energy band becomes distinct. In order to highlight this feature, the valence band tops of the four models are shifted to take the same energy level in Fig. 4(c). In this figure, it is evident that the Slab\_ $V_I$ -2 model has a discrete energy level within the band gap. As shown in Fig. 5, this level is assigned to the orbital localized at the  $V_I$  in Slab1\_ $V_I$ -2. It should be noted that the orbital shape clearly shows the bonding character of the  $\text{Pb}_2$  dimer at the position of the  $V_I$ . Therefore, we can conclude that the discrete level is due to electron localization at the  $V_I$  on which bonding interaction occurs between the two adjacent Pb atoms. In the other Slab1\_ $V_I$  models, the DOS data do not imply charge localization. This is consistent with the nearly unchanged Pb–Pb distance discussed above.

Since the electron localization results in the mid-gap level and the shortening of the adjacent Pb–Pb distance, it seems interesting to investigate the influence of excess charge doped in the present system. Zhang *et al.* reported that two Pb atoms of  $\text{MAPbI}_3$  around an intrinsic  $V_I$  can form a dimer when an extra electron is captured into the defective system.<sup>8</sup> Since this suggests that the charge state would play an essential role in structural distortion near the  $V_I$  site, the Hirshfeld charge distribution of perfect and defective perovskite models were examined. In comparison with the defect-free  $\text{MAPbI}_3$  slab, we found that the total electron density of the two Pb atoms around the  $V_I$  increases by 0.15 e (e: electrons) in Slab1\_ $V_I$ -2 (0.09 and 0.06 e for the Pb in the first and second layers, respectively). For other neutral  $V_I$ -containing slabs, the increase of the electron population on the two dangling Pb atoms is only 0.04 e, 0.08 e,



Fig. 3 Calculated total density of states (TDOS) of the defect-free Slab1. The insets indicate the orbital shape of band edges.





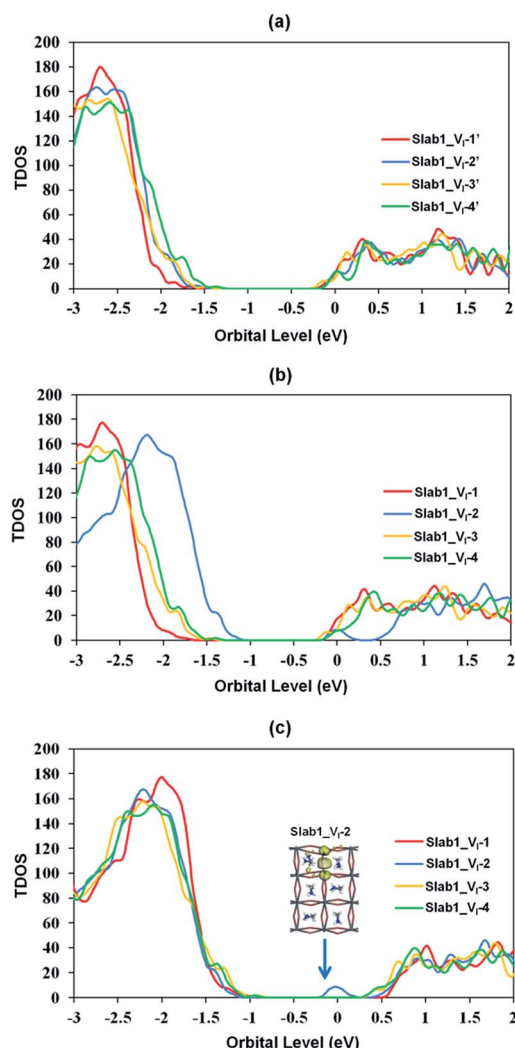


Fig. 4 Calculated total density of states (TDOS) of the  $V_I$ -containing  $\text{MAPbI}_3$  slab models (a) before geometry optimization, (b) after geometry optimization, and (c) after geometry optimization where the valence band tops of all the defective slab models were adjusted to the same level. The inset in (c) indicates the orbital shape.

and 0.06 e in Slab1\_ $V_I$ -1, Slab1\_ $V_I$ -3, and Slab1\_ $V_I$ -4, respectively (Fig. S6 of the ESI†). It is evident that the dimerization can be related to electron localization. A similar feature was pointed out by Zhang.<sup>8</sup>

To further uncover the influence of charge localization in the defective system, geometry optimizations were performed on the positively and negatively charged  $V_I$ -containing  $\text{MAPbI}_3$ . As shown in Fig. S7–S10 of the ESI†, when one electron is doped, dimerization of Pb around the defective site is observed not only in Slab1\_ $V_I$ -2<sup>−</sup> but also in Slab1\_ $V_I$ -3<sup>−</sup> and Slab1\_ $V_I$ -4<sup>−</sup>. The calculated Pb–Pb distances are 3.575 Å (Fig. S8†), 3.523 Å (Fig. S9†), and 3.527 Å (Fig. S10†), respectively. These data indicate that the  $V_I$  functions as an electron trap at the interface in perovskite solar cells. The present data imply that the  $V_I$  in the inner region (away from the surface) would capture an electron when the electron concentration is high in a photovoltaic device.

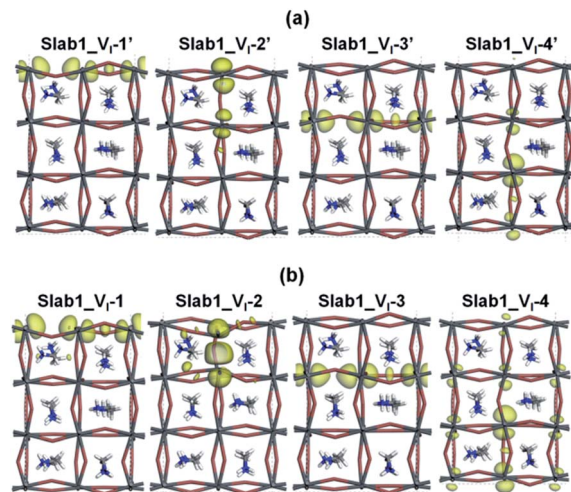


Fig. 5 The orbital shape of the conduction band edges (isovalue: 0.015 a.u.) of (a) the  $V_I$ -containing  $\text{MAPbI}_3$  slab model before geometry optimization and (b) the  $V_I$ -containing  $\text{MAPbI}_3$  slab model after geometry optimization.

In contrast, when the defective  $\text{MAPbI}_3$  models are positively (+1) charged, the Pb–Pb dimer does not form in any case (see Fig. S7–S10 of the ESI†). This suggests that the formation of the Pb–Pb dimer around the  $V_I$  is strongly related not to hole localization but to electron localization in defective metal halide perovskites. Therefore, we can conclude that the  $V_I$  would cause lowering of the energy conversion efficiency in perovskite solar cells by electron trapping. This lattice defect would be problematic, in particular, at the interface with the electron transport layer.

Next, we focused on graphene (G) +  $\text{MAPbI}_3$  hybrid systems by using the above-mentioned slab models in order to investigate the impact of coating graphene on geometrical and electronic structure modifications of defective perovskites. Here a single-layered graphene cell containing 60 carbon atoms was used to coat the perovskite surface (see the computational details). The optimized perfect/defective G +  $\text{MAPbI}_3$  hybrid structures are depicted in Fig. 6.

Two remarkable geometrical characteristics can be detected. In comparison with the bare state (Fig. 2), the  $\text{PbI}_2$  surface of  $\text{MAPbI}_3$  is flattened in the presence of the graphene coat, which can be elucidated by interfacial interactions consisting of both Pb– $\pi$  and I– $\pi$  effects. A similar surface modification has been reported in the case of hybridization between graphene and a defect-free  $\gamma$ - $\text{MAPbI}_3$ .<sup>55</sup> The other feature is that the  $\text{Pb}_2$  dimer of the defective Slab1\_ $V_I$ -2 model is broken after graphene binding, with an extended Pb–Pb distance of 6.806 Å. It should be noted that the cleavage of Pb–Pb was also observed in the case of negatively charged Slab1\_ $V_I$ -2<sup>−</sup>. However, for the negatively charged Slab1\_ $V_I$ -4<sup>−</sup> in which the dimer resides in the bulk position, the Pb–Pb segment still exists with the incorporation of graphene (Fig. S11 and S12 of the ESI†). These results suggest that the stretching of Pb–Pb can be attributed to the surface Pb– $\pi$  interactions.





Fig. 6 (a) Defect-free and (b)  $V_I$ -containing defective graphene +  $\text{MAPbI}_3$  hybrids.

The binding energies of complexes ( $E_b = E(\text{Slab1}) + E(\text{G}) - E(\text{hybrid})$ ) are listed in Table S3 of the ESI†. The results reveal that the hybridization is an exothermic process and the calculated  $E_b$  values among different perovskite slabs are very similar, implying that the introduction of a single I vacancy does not modify the interface stability remarkably. In addition, we investigated the distortion energy ( $E_d$ ) of the perovskite and graphene after hybridization. The results collected in Table S3 of the ESI† showed that the structural distortion of graphene is very small ( $<0.03$  eV) whereas the modification on the perovskite is significant ( $>0.1$  eV). The deformation of  $\text{MAPbI}_3$  is mainly attributed to the flattened surface as mentioned before, and in particular, the  $E_d$  of  $\text{Slab1}_{V_I-2}$  (0.347 eV) is much larger than that of other models because of the energy requirement for Pb–Pb dimer cleavage, which can be further confirmed by the calculated pair formation energy ( $E_p$ ) of the Pb–Pb dimer (0.371 eV) shown in Table S4 of the ESI†.

In order to explain the modification of perovskites after binding with graphene, the electron distributions of the hybrid systems were further investigated. The calculated Hirshfeld charge shows that the perovskite acts as an electron donor as shown in Table 1. The total number of electrons transferred

from  $\text{Slab1}$ ,  $\text{Slab1}_{V_I-1}$ ,  $\text{Slab1}_{V_I-2}$ ,  $\text{Slab1}_{V_I-3}$ , and  $\text{Slab1}_{V_I-4}$  is 0.20, 0.37, 0.34, 0.20, and 0.23 e, respectively. This indicates two characteristics of the graphene layer. One is that graphene functions as a hole-injecting material. This is due to the fact that the Fermi level of graphene is located at the bottom of the conduction band of the defective  $\text{MAPbI}_3$  layer. Another characteristic is that more electrons are injected into graphene when the  $V_I$  exists on the surface. This is because the surface state (or the surface/subsurface Pb atoms) would be more influenced by the  $V_I$  in comparison with the bulk state (or the Pb atoms in the bulk).

It is interesting to see the change of electron distribution of the two dangling Pb atoms around the  $V_I$  before and after the graphene coating (Fig. S6 and S13 of the ESI†). In  $\text{Slab1}_{V_I-2}$  having the Pb–Pb dimer, 0.34 e are removed from  $\text{MAPbI}_3$ : 0.21 e are taken from the dimer, while 0.13 e are taken from the rest of the crystal. On the other hand, in  $\text{Slab1}_{V_I-1}$ , 0.37 e are removed from the perovskite layer. Only 0.06 e are taken from the dangling Pb atoms, while 0.31 e are taken from the rest of the crystal. This indicates that the hole injected into the two slab models distributes over the lattice and the electron localization on the dangling Pb seen in  $\text{Slab1}_{V_I-2}$  is relaxed.

The electron density difference (EDD) of the G +  $\text{MAPbI}_3$  hybrids (defined as  $\text{EDD} = \rho(\text{hybrid}) - \rho(\text{Slab1}) - \rho(\text{G})$ ) also suggests that the interactions between graphene and the unsaturated Pb atoms on the surface of either  $\text{Slab1}_{V_I-1}$  or  $\text{Slab1}_{V_I-2}$  are much stronger than those observed in the other systems (Fig. 7). In  $\text{Slab1}_{V_I-2}$ , we see that the Pb atom just above the  $V_I$  is largely oxidized by graphene. This implies that the local cation– $\pi$  interaction on the dangling Pb atom on the top layer would occur. This enhanced local interaction would be the reason for the healing effect (removal of the dimer) around the  $V_I$ .

Since the Pb–Pb dimer, which was proved to be the origin of trap level formation, can be effectively removed by introducing a graphene layer, the electronic properties of  $\text{MAPbI}_3$  slabs were expected to be altered accordingly in the presence of graphene.

Table 1 Hirshfeld charge of the defect-free G +  $\text{Slab1}$  and G +  $\text{Slab1}_{V_I}$  hybrids. Values in parentheses indicate the charge without graphene

Structure	Graphene	$\text{Slab1}_{V_I}$	
		Dangling Pb atoms	The rest in total
G + $\text{Slab1}$	−0.20	(+0.57) <sup>a</sup>	(−0.57)
G + $\text{Slab1}_{V_I-1}$	−0.37	+0.67(+0.61)	−0.30(−0.61)
G + $\text{Slab1}_{V_I-2}$	−0.34	+0.66(+0.45)	−0.32(−0.45)
G + $\text{Slab1}_{V_I-3}$	−0.20	+0.43(+0.43)	−0.23(−0.43)
G + $\text{Slab1}_{V_I-4}$	−0.23	+0.45(+0.44)	−0.22(−0.44)

<sup>a</sup> Averaged value (0.285 e per one Pb atom).





Fig. 7 Electron density difference of the (a) defect-free and (b)  $V_I$ -containing graphene +  $\text{MAPbI}_3$  hybrids (isovalue: 0.003 a.u.). Purple and cyan represent accumulation and depletion of electrons, respectively.

As shown in Fig. 8, on the one hand, the calculated partial density of states (PDOS) of  $\text{MAPbI}_3$  in the  $\text{G} + \text{MAPbI}_3$  hybrid showed that the surface flattening leads to insignificant changes of state distributions for the defect-free as well as  $V_I$ -containing  $\text{MAPbI}_3$  slabs without  $\text{Pb-Pb}$  dimers (Slab1 and defective Slab1\_ $V_I$ -1, -3, and -4). On the other hand, as expected, because of the removal of the  $\text{Pb}_2$  dimer, the deep-level defect within the band gap in Slab1\_ $V_I$ -2 (Fig. 4) is eliminated after hybridization with graphene. Clearly, it can be concluded that, because of interfacial electron transfer, the unfavored  $\text{Pb}_2$  dimer of the defective perovskite with a single  $V_I$  is broken by the graphene coating, which leads to the “healing” of trap levels of defective  $\text{MAPbI}_3$ . Such a trap passivation effect is crucial to depress carrier recombination and is believed to be an effective strategy to enhance the photovoltaic performance of PSC devices. Aromatic or, at least,  $\pi$ -conjugated compounds would be promising as surface coating materials for electron-trap passivation. From the viewpoint of coordination chemistry, any molecules that can strongly coordinate onto the  $\text{Pb}$  atom would also function as materials having the healing effect.

### 3.2. $\text{MAPbI}_3$ with a $\text{Pb}$ vacancy

A single  $\text{Pb}$  vacancy ( $V_{\text{Pb}}$ ) is another defect which might exist in  $\text{MAPbI}_3$ . When a neutral  $\text{Pb}$  atom is removed to form a  $V_{\text{Pb}}$  in the bulk, the DFT optimization showed that the six neighboring  $\text{I}$  atoms change their positions slightly as shown in Fig. S4 of the ESI,<sup>†</sup> but the change is not so appreciable: the average distance between the two adjacent  $\text{I}$  atoms is 4.404 Å (change of  $-2.7\%$ ), which is close to that in the perfect crystal (4.528 Å). The calculated DOS suggests that the  $V_{\text{Pb}}$  in bulk  $\text{MAPbI}_3$  acts as a shallow acceptor because some holes are generated in the valence band as seen in Fig. S5 of the ESI.<sup>†</sup> This p-type characteristic has already been pointed out by Kim *et al.*<sup>35</sup>

Concerning slab models having a  $V_{\text{Pb}}$ , two types of configurations are possible: the  $V_{\text{Pb}}$  may appear on the surface or in the bulk as depicted in Fig. 9(b). Here, these models are called



Fig. 8 Calculated partial density of states (PDOS) of  $\text{MAPbI}_3$  in the graphene +  $\text{MAPbI}_3$  hybrids: (a) defect-free and (b)  $V_I$ -containing models, and (c) the orbital shape corresponds to the conduction band edges of  $\text{MAPbI}_3$  (isovalue: 0.015 a.u.).







Fig. 9 (a) Defect-free and (b)  $V_{\text{Pb}}$ -containing defective  $\text{MAPbI}_3$  slabs.

Slab1\_ $V_{\text{Pb}}$ -1 and Slab1\_ $V_{\text{Pb}}$ -2, respectively. Although they have a common defect, *i.e.*  $V_{\text{Pb}}$ , the optimized structures are significantly different as shown in the upper panel of Fig. 9(b): removal of a surface Pb atom (Slab1\_ $V_{\text{Pb}}$ -1) leads to the formation of an I–I dimer having an interatomic distance of 2.778 Å. Such a short I–I distance was also obtained in the larger slab model (Slab4) as shown in Fig. S3(b).<sup>†</sup> In contrast, in Slab1\_ $V_{\text{Pb}}$ -2, the inner  $V_{\text{Pb}}$  produces 6 dangling I atoms without any dimerization of the two neighboring I atoms, namely, the structural feature inside the  $\text{MAPbI}_3$  slab is essentially similar to that in the bulk.

The DOSs of Slab1\_ $V_{\text{Pb}}$ -1 and Slab1\_ $V_{\text{Pb}}$ -2 also show a marked difference (Fig. 10(b) and (c)). After geometry optimization, the former has a discrete mid-gap level, while the latter does not. The DOS spectra of the two systems before optimization (Fig. 10(a)) indicate that, without structural reorganization, the two spectra of the valence band are almost identical. After the geometry optimization, the top region of the valence band of Slab1\_ $V_{\text{Pb}}$ -1 splits to generate the discrete level pointed out above. After the band splitting, the valence band after optimization becomes completely filled with electrons. It is interesting to note that the DOS of the conduction band does not change its shape even after geometry optimization. This supports the view that the mid-gap level originated from the valence band.

The change in the DOS of Slab1\_ $V_{\text{Pb}}$ -1 implies that the defect center would be positively charged. The calculated Hirshfeld charge shows that the net charge of the dimerized  $\text{I}_2$  center is  $-0.52$  (see Table 2) which is much smaller than that of the defect-free system. On the surface of the latter, the total net charge of two surface I atoms is  $-0.91$ : 0.39 electrons are taken from the two I atoms and are transferred to the other region of the crystal (see Fig. S14 of the ESI<sup>†</sup>). This indicates that the  $V_{\text{Pb}}$  acts as a hole trap because the  $\text{I}_2$  dimer formation is possible though bonding interaction between the two adjacent I atoms as shown in Fig. 11.

It seems reasonable to expect that further hole doping would result in  $\text{I}_2$  dimer formation even in the inner region



Fig. 10 Calculated total density of states (TDOS) of the  $V_{\text{Pb}}$ -containing  $\text{MAPbI}_3$  slab models (a) before geometry optimization, (b) after geometry optimization, and (c) after geometry optimization where the valence band tops of all the defective slab models were adjusted to the same level. The inset in (c) indicates the orbital shape.

(Slab1\_ $V_{\text{Pb}}$ -2) as has been observed for the  $V_{\text{I}}$ . Unexpectedly, additional hole doping did not result in dimer formation in this inner defect model as shown in Fig. S16(d) of the ESI.<sup>†</sup> The hole

Table 2 Hirshfeld charge of the G + Slab1\_ $V_{\text{Pb}}$  hybrids. Values in parentheses indicate the charge without graphene

Structure	Graphene	Slab1_ $V_{\text{Pb}}$	
		Dangling I atoms <sup>a</sup>	The rest in total
G + Slab1	$-0.20$	$(-0.91/-1.09)^b$	$(+0.91/+1.09)$
G + Slab1_ $V_{\text{Pb}}$ -1	$+0.14$	$-0.78(-0.52)$	$+0.64(+0.52)$
G + Slab1_ $V_{\text{Pb}}$ -2	$+0.07$	$-0.99(-0.97)$	$+0.92(+0.97)$

<sup>a</sup> Sum of five (or six) iodine atoms in G + Slab1\_ $V_{\text{Pb}}$ -1 (or G + Slab1\_ $V_{\text{Pb}}$ -2). <sup>b</sup> Calculated from the average charge ( $-0.18$  e per I atom) and the number of dangling I atoms.  $-0.91$  e ( $-1.09$  e) is for the five (six) dangling atoms.





Fig. 11 The orbital shape of the valence band edges (isovalue: 0.015 a.u.) of the  $V_{\text{Pb}}$ -containing  $\text{MAPbI}_3$  slab models (a) before and (b) after geometry optimization.

trapping character of the  $V_{\text{Pb}}$  also suggests that electron doping into  $\text{Slab1\_VPb-1}$  should break the dimer. The optimized geometries of such systems (singly and doubly electron-doped ones) clearly show the elongation of the I–I distance as seen in Fig. S15 of the ESI†. This observation also justifies the hole-doped character of the surface I–I dimer.

Since we have observed substantial effect of graphene coating on the electronic structure of the defective  $\text{MAPbI}_3$ , the corresponding hybrid structures represented as  $\text{G} + \text{Slab1\_VPb-1}$  and  $\text{G} + \text{Slab1\_VPb-2}$  were also investigated. The optimized structures in Fig. 12 (see also Fig. S17 of the ESI†) clearly show that, in this hybrid system, the  $\text{I}_2$  dimer does not form on the surface. The calculated PDOS for the  $\text{MAPbI}_3$  moiety (Fig. 13) is similar to that of the bulk: no mid-gap level appears even in  $\text{Slab1\_VPb-1}$ . Therefore, we conclude that graphene has a healing effect even for removing the hole trap.



Fig. 12 (a) Defect-free and (b)  $V_{\text{Pb}}$ -containing defective graphene +  $\text{MAPbI}_3$  hybrids.



Fig. 13 (a) Calculated partial density of states (PDOS) of  $\text{MAPbI}_3$  in the  $V_{\text{Pb}}$ -containing graphene +  $\text{MAPbI}_3$  hybrids, and (b) the orbital shape of the valence band edges of  $\text{MAPbI}_3$  (isovalue: 0.015 a.u.).

In order to analyse the driving force for the cleavage of the I–I dimer by graphene, we investigated the Hirshfeld charge of the pristine perovskites and hybrid structures and the results are tabulated in Table 2. We see that the Hirshfeld charge of graphene in the hybrids is positive (+0.14 e and +0.07 e in  $\text{G} + \text{Slab1\_VPb-1}$  and  $\text{G} + \text{Slab1\_VPb-2}$ , respectively). This is different from the electron-accepting character of graphene (−0.20 e, Table 2) in the defect-free system, which may result from the p-type doping with the  $V_{\text{Pb}}$  as mentioned. The electron-donating character is also proved by the calculated EDD distributions shown in Fig. 14: the electrons are extracted from the attached graphene layer to the  $V_{\text{Pb}}$ -containing  $\text{MAPbI}_3$ .

The Hirshfeld charge distribution clarifies the role of the graphene on the surface. The sum of the net charges of the five dangling I atoms in  $\text{Slab1\_VPb-1}$  is −0.52 e, while it becomes −0.78 e after graphene coating (see also Fig. S14 and S18 for details†). In the difference (0.26 e), 0.14 e are provided by graphene, and 0.12 e are transferred from the rest of the crystal. Therefore, graphene plays two roles: one is to provide electrons to the hole-trapping site, and the other is to reorganize the charge distribution in the crystal. Through comparison with  $\text{Slab1\_VPb-2}$ , we find that the surface vacancy always has a larger influence on charge redistribution.

### 3.3. $\text{MAPbI}_3$ with a MA vacancy

We also investigated the MA vacancy ( $V_{\text{MA}}$ ) in  $\text{MAPbI}_3$ . The calculated DOS (Fig. S5(d) of the ESI†) shows that the  $V_{\text{MA}}$  in the bulk  $\text{MAPbI}_3$  acts as a p-type doping defect and produces a shallow-level defect near the band edge. This feature is similar to that of the  $V_{\text{Pb}}$  in the bulk  $\text{MAPbI}_3$  model.







Fig. 14 Electron density difference of the  $V_{\text{Pb}}$ -containing graphene +  $\text{MAPbI}_3$  hybrids (isovalue: 0.003 a.u.). Purple and cyan represent accumulation and depletion of electrons, respectively.

For the perovskite slabs with a single  $V_{\text{MA}}$ , two defective models with different  $V_{\text{MA}}$  locations were calculated (Fig. 15). The calculated DOS in Fig. 16 reveals that the  $V_{\text{MA}}$  of  $\text{MAPbI}_3$  slabs always shows a shallow-level defect near the band edge. Therefore, it can be concluded that the trap center in perovskites forms only when the  $\text{PbI}_6$  octahedral unit is deformed (*i.e.*  $V_1$  or  $V_{\text{Pb}}$ ).

In contrast, the A-site single vacancy, *e.g.*  $V_{\text{MA}}$ , shows a high defect tolerance character no matter how the vacancy resides around the surface or in the bulk position. In the presence of graphene, a compressed  $\text{PbI}_2$  surface is observed (Fig. 17) and the modification in the PDOS of defective  $\text{MAPbI}_3$  is insignificant (Fig. 18). In addition, similar to the defective perovskite with a  $V_{\text{Pb}}$ , the cationic defect and excess hole doping results in an electron deficient character of the perovskite. Graphene acts as an electron donor in the hybrid structure, which can be proved by the Hirshfeld charge (+0.10 and +0.09 e of graphene



Fig. 16 (a) Calculated total density of states (TDOS) of  $V_{\text{MA}}$ -containing  $\text{MAPbI}_3$ , and (b) the orbital shape of the valence band edges of  $\text{MAPbI}_3$  (isovalue: 0.015 a.u.).

in  $\text{G} + \text{Slab1}_{V_{\text{MA}}-1}$  and  $\text{G} + \text{Slab1}_{V_{\text{MA}}-2}$ , respectively, Table S5 of the ESI†) and the visualized EDD shown in Fig. 19.

### 3.4. Molecules showing the healing effect

So far, we have shown that graphene has a healing effect that suppresses electron- and hole-trapping due to I and Pb vacancies on the surface of  $\text{MAPbI}_3$ . It seems interesting to investigate what other chemicals would also show the healing effect. Since aromatic  $\pi$  electrons can interact with ions, aromatic compounds would be an alternative to graphene. It is also interesting to investigate non-aromatic unsaturated hydrocarbons



Fig. 15 (a) Defect-free and (b)  $V_{\text{MA}}$ -containing defective  $\text{MAPbI}_3$  slabs.

Fig. 17 (a) Defect-free and (b)  $V_{\text{MA}}$ -containing defective graphene +  $\text{MAPbI}_3$  hybrids.



Fig. 18 (a) Calculated partial density of states (PDOS) of MAPbI<sub>3</sub> in the V<sub>MA</sub>-containing graphene + MAPbI<sub>3</sub> hybrids, and (b) the orbital shape of the valence band edges of MAPbI<sub>3</sub> (isovalue: 0.015 a.u.).

in order to highlight the importance of  $\pi$  electrons. Small molecules forming Werner complexes on the Pb center are also interesting. In experiments, coating with organic molecules (such as C<sub>5</sub>H<sub>5</sub>N) has also been investigated and has been shown to improve the device performance.<sup>56</sup>

Herein CH<sub>4</sub>, C<sub>2</sub>H<sub>4</sub>, C<sub>6</sub>H<sub>6</sub>, and C<sub>5</sub>H<sub>5</sub>N were selected as the first candidates for the experiments. In order to reduce computational cost, here we employed a smaller MAPbI<sub>3</sub> slab (Fig. S1 of the ESI†, labelled Slab2) to study the molecular adsorption.



Fig. 19 Electron density difference of the V<sub>MA</sub>-containing graphene + MAPbI<sub>3</sub> hybrids (isovalue: 0.003 a.u.). Purple and cyan represent accumulation and depletion of electrons, respectively.

Note that the Slab2 model showed similar defective properties (Pb or I dimer formation around the surface and the corresponding trap-level defects) and the healing effect of graphene (Fig. S19–S23 of the ESI†). Here Slab2\_V<sub>I</sub>-2 with a Pb–Pb dimer and Slab2\_V<sub>Pb</sub>-1 with an I–I dimer (Fig. S19 of the ESI†) were employed as defective perovskite models.

In the case of Slab2\_V<sub>I</sub>-2 with a dimerized Pb segment, the Pb–Pb dimer was removed when C<sub>2</sub>H<sub>4</sub>, C<sub>6</sub>H<sub>6</sub>, or C<sub>5</sub>H<sub>5</sub>N was adsorbed onto the surface (see Fig. 20). The calculated DOS further confirmed that the deep-level defects of those defective MAPbI<sub>3</sub> vanished (Fig. 21). It should be noted that the dimerized Pb was always broken when the configuration of C<sub>5</sub>H<sub>5</sub>N is face-on (C<sub>5</sub>H<sub>5</sub>N(f) + Slab2\_V<sub>I</sub>-2) or edge-on (C<sub>5</sub>H<sub>5</sub>N(e) + Slab2\_V<sub>I</sub>-2). In the case of C<sub>2</sub>H<sub>4</sub>, C<sub>6</sub>H<sub>6</sub>, and C<sub>5</sub>H<sub>5</sub>N with a face-on orientation, the calculated Hirshfeld charge on the dimerized Pb–Pb dimer is reduced by 0.10, 0.13, and 0.08 e, respectively, giving rise to the charge delocalization and the cleavage of the Pb<sub>2</sub> dimer (Fig. 21 and S24 of the ESI†). On the other hand, for the end-on C<sub>5</sub>H<sub>5</sub>N, the molecule is adsorbed *via* lone-pair interactions between N and the Pb on the defective site (4-coordinated originally). The N–Pb distance is as short as 2.541 Å. Consequently, this 4-coordinated Pb becomes 5-coordinated which is the same as that observed for other Pb atoms on the surface without defects. Therefore, we see that when the electron distribution is delocalized the dimer formation is suppressed.

Motivated by the observations, we further studied the H<sub>2</sub>O + Slab2\_V<sub>I</sub>-2 (Fig. 20) hybrid. As expected, because of a similar lone pair interaction between the O of H<sub>2</sub>O and the Pb on the defective site, the attached H<sub>2</sub>O can also disrupt the Pb–Pb dimer with an elongated distance of 5.405 Å. Therefore, water molecules are effective in removing the deep-level defects caused by Pb–Pb dimers (Fig. 21 and S24 of the ESI†), which can be used to explain the previous experimental evidence, that is, the sprayed water molecules result in decreased defect density and improved device efficiencies.<sup>57,58</sup>

So far, we have assumed that the perovskite layer was prepared under PbI<sub>2</sub>-rich conditions because a stronger interaction with graphene is expected. This is also justified by the experiment suggesting that the PbI<sub>2</sub>-terminated MAPbI<sub>3</sub> provides an improved photo-carrier transport and higher performance.<sup>59–62</sup> However, the existence of the MAI-terminated surface cannot be excluded since the surface composition of the perovskite can be modulated by synthesis procedures. In addition, the MAI layer at the grain boundaries of MAPbI<sub>3</sub> was reported as a healing layer to improve the carrier lifetime and suppress the charge recombination at the interfaces.<sup>63</sup> Therefore we also investigated a MAI-terminated perovskite slab model with a single V<sub>I</sub> (Fig. S25 of the ESI†). The optimized geometry showed that the Pb–Pb dimer does not form and has a large interatomic distance of 6.980 Å (Fig. S26 and S27 of the ESI†) in the Slab5\_V<sub>I</sub>-4 model which is comparable to that in the Slab1\_V<sub>I</sub>-2 model. This result indicates that the surface with MAI would not have electron traps. This is consistent with the previous conclusions experimentally obtained.<sup>59–62</sup>

For the defective MAPbI<sub>3</sub> with an I–I dimer, which is predicted for the system with the surface V<sub>Pb</sub>, the present calculation predicts that the selected molecules or MAI does not give





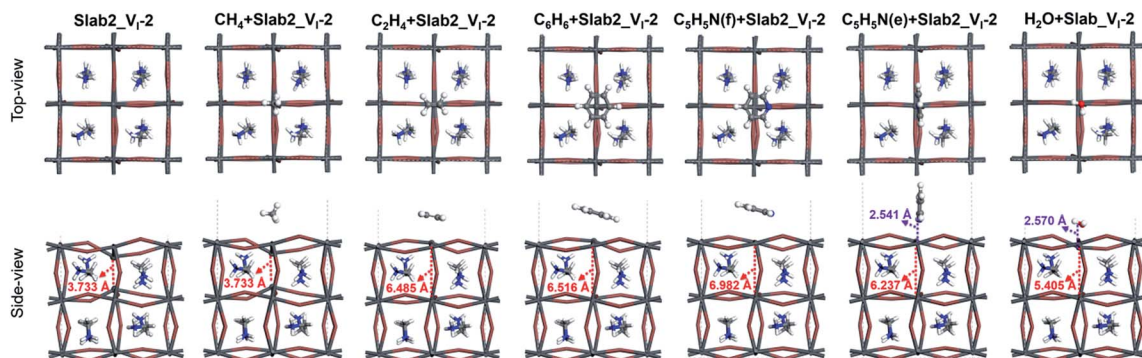


Fig. 20 Defective MAPbI<sub>3</sub> slabs (Slab2\_VI-2) and the corresponding molecule + MAPbI<sub>3</sub> hybrids.



Fig. 21 Calculated partial density of states (PDOS) of the molecule + VI-containing MAPbI<sub>3</sub> (Slab2\_VI-2) hybrids. (a) presents the original data and (b) presents the adjusted data in which the valence band tops of all the slab models were adjusted to the same level for clarity.

the healing effect. This may be due to the poor electron donating abilities of these species: the dimerized I<sub>2</sub> still exists upon coordination of these molecules even after adsorption (Fig. S26 and S28 of the ESI†). Therefore, we can conclude that graphene exhibits healing effects on electron- and hole-traps due to single vacancies. This implies that the introduction of the graphene layer would be beneficial to both surfaces of metal halide perovskite layers connected to electron- and hole-transporting materials. The present results also imply that the use of  $\pi$ -conjugated compounds like fullerene and spiro-OMeTAD would be very reasonable because both of them would also have a healing effect to remove carrier traps at the interface in perovskite solar cells.

## 4 Conclusions

In this study, we have investigated the geometries and electronic structures of the surfaces of the MAPbI<sub>3</sub> perovskite compound with single vacancies by using first-principles calculations. We have also studied the impact of surface fabrication using graphene because energy conversion devices using this material have a multi-layered structure.

The present computation predicts that Pb and I vacancies beneath the surface can function as carrier traps. The appearance of the mid-gap levels near the vacancies is due to the formation of the I–I and Pb–Pb dimers, respectively. This characteristic of the defective material is considered to degrade the performance of energy conversion devices using MAPbI<sub>3</sub>. This feature would be quite unique only in the surface region: in the bulk, such dimers would not form, as suggested by Zhang *et al.*<sup>8</sup> The MA vacancy is considered to be harmless in electronic devices.

Through the investigation of the surface fabrication using graphene, we have found that the undesirable I–I and Pb–Pb dimers do not form in the stable geometries in the defective systems. This is because charge localization at a Pb/I single vacancy is suppressed by graphene. This characteristic indicates that graphene has a “healing effect” against carrier trapping by the vacancy. This healing effect has also been predicted for surface coating with unsaturated hydrocarbons, but graphene is more beneficial because it is effective in eliminating any kind of carrier trapping. The origin of the healing effect would be electronic interaction on the surface providing electrons/holes to suppress the formation of the carrier traps. It also plays a role in preventing charge localization at the trapping sites around a single vacancy.

## Conflicts of interest

There are no conflicts to declare.

## Acknowledgements

This research was financially supported by the New Energy and Industrial Technology Development Organization (NEDO) project and by a Grant-in-Aid for Scientific Research on Innovative Areas “ $\pi$ -Figuration” (JSPS KAKENHI 26102015 for M. S.).





## Notes and references

- M. R. Filip, G. E. Eperon, H. J. Snaith and F. Giustino, *Nat. Commun.*, 2014, **5**, 5757.
- W.-J. Yin, T. Shi and Y. Yan, *Adv. Mater.*, 2014, **26**, 4653.
- G. Xing, N. Mathews, S. Sun, S. S. Lim, Y. M. Lam, M. Grätzel, S. Mhaisalkar and T. C. Sum, *Science*, 2013, **342**, 344.
- A. Kojima, K. Teshima, Y. Shirai and T. Miyasaka, *J. Am. Chem. Soc.*, 2009, **131**, 6050.
- NREL, Best Research-Cell Efficiencies, <https://www.nrel.gov/pv/assets/images/efficiency-chart.png>.
- W. Shockley and H. J. Queisser, *J. Appl. Phys.*, 1961, **32**, 510.
- J. M. Ball and A. Petrozza, *Nat. Energy*, 2016, **1**, 16149.
- M. L. Agiorgousis, Y. Y. Sun, H. Zeng and S. Zhang, *J. Am. Chem. Soc.*, 2014, **136**, 14570.
- T. Tachikawa, I. Karimata and Y. Kobori, *J. Phys. Chem. Lett.*, 2015, **6**, 3195.
- Y. Yamada, T. Yamada, A. Shimazaki, A. Wakamiya and Y. Kanemitsu, *J. Phys. Chem. Lett.*, 2016, **7**, 1972.
- T. S. Sarker, C. Momblona, L. Gil-Escrig, H. J. Bolink and L. J. A. Koster, *Adv. Energy Mater.*, 2017, **7**, 1602432.
- Y. Shao, Y. Fang, T. Li, Q. Wang, Q. Dong, Y. Deng, Y. Yuan, H. Wei, M. Wang, A. Gruverman, J. Shialda and J. Huang, *Energy Environ. Sci.*, 2016, **9**, 1752.
- X. Wu, M. T. Trinh, D. Niesner, H. Zhu, Z. Norman, J. S. Owen, O. Yaffe, B. J. Kudisch and X.-Y. Zhu, *J. Am. Chem. Soc.*, 2015, **137**, 2089.
- J. Kang and L.-W. Wang, *J. Phys. Chem. Lett.*, 2017, **8**, 489.
- Y. Liu, Z. Yang, D. Cui, X. Ren, J. Sun, X. Liu, J. Zhang, Q. Wei, H. Fan, F. Yu, X. Zhang, C. Zhao and S. Liu, *Adv. Mater.*, 2015, **27**, 5176.
- Y. Shao, Z. Xiao, C. Bi, Y. Yuan and J. Huang, *Nat. Commun.*, 2014, **5**, 5784.
- J. Xu, A. Buin, A. H. Ip, W. Li, O. Voznyy, R. Comin, M. Yuan, S. Jeon, Z. Ning, J. J. McDowell, P. Kanjanaboos, J. P. Sun, X. Lan, L. N. Quan, D. H. Kim, I. G. Hill, P. Maksymovych and E. H. Sargent, *Nat. Commun.*, 2015, **6**, 7081.
- C.-H. Chiang and C.-G. Wu, *Nat. Photonics*, 2016, **10**, 196.
- A. Abate, M. Saliba, D. J. Hollman, S. D. Stranks, K. Wojciechowski, R. Avolio, G. Grancini, A. Petrozza and H. J. Snaith, *Nano Lett.*, 2014, **14**, 3247.
- N. K. Noel, A. Abate, S. D. Stranks, E. S. Parrott, V. M. Burlakov, A. Goriely and H. J. Snaith, *ACS Nano*, 2014, **8**, 9815.
- F. Wang, W. Geng, Y. Zhou, H. H. Fang, C. J. Tong, M. A. Loi, L. M. Liu and N. Zhao, *Adv. Mater.*, 2016, **28**, 9986.
- S. Ye, H. Rao, Z. Zhao, L. Zhang, H. Bao, W. Sun, Y. Li, F. Gu, J. Wang, Z. Liu, Z. Bian and C. Huang, *J. Am. Chem. Soc.*, 2017, **139**, 7504.
- Q. Chen, H. Zhou, T. B. Song, S. Luo, Z. Hong, H. S. Duan, L. Dou, Y. Liu and Y. Yang, *Nano Lett.*, 2014, **14**, 4158.
- T. S. Sarker, C. Momblona, L. Gil-Escrig, J. Ávila, M. Sessolo, H. J. Bolink and L. J. A. Koster, *ACS Energy Lett.*, 2017, **2**, 1214.
- J.-S. Yeo, C.-H. Lee, D. Jang, S. Lee, S. M. Jo, H.-I. Joh and D.-Y. Kim, *Nano Energy*, 2016, **30**, 667.
- Z. Zhu, J. Ma, Z. Wang, C. Mu, Z. Fan, L. Du, Y. Bai, L. Fan, H. Yan, D. L. Phillips and S. Yang, *J. Am. Chem. Soc.*, 2014, **136**, 3760.
- J. T.-W. Wang, J. M. Ball, E. M. Barea, A. Abate, J. A. Alexander-Webber, J. Huang, M. Saliba, I. Mora-Sero, J. Bisquert, H. J. Snaith and R. J. Nicholas, *Nano Lett.*, 2014, **14**, 724.
- G. S. Han, Y. H. Song, Y. U. Jin, J.-W. Lee, N.-G. Park, B. K. Kang, J.-K. Lee, I. S. Cho, D. H. Yoon and H. S. Jung, *ACS Appl. Mater. Interfaces*, 2015, **7**, 23521.
- Q. Luo, Y. Zhang, C. Liu, J. Li, N. Wang and H. Lin, *J. Mater. Chem. A*, 2015, **3**, 15996.
- W. Li, H. Dong, X. Guo, N. Li, J. Li, G. Niu and L. Wang, *J. Mater. Chem. A*, 2014, **2**, 20105.
- K. Yan, Z. Wei, J. Li, H. Chen, Y. Yi, X. Zheng, X. Long, Z. Wang, J. Wang, J. Xu and S. Yang, *Small*, 2015, **11**, 2269.
- Y. Jiao, F. Ma, G. Gao, H. Wang, J. Bell, T. Frauenheim and A. Du, *RSC Adv.*, 2015, **5**, 82346.
- Z. Wu, S. Bai, J. Xiang, Z. Yuan, Y. Yang, W. Cui, X. Gao, Z. Liu, Y. Jin and B. Sun, *Nanoscale*, 2014, **6**, 10505.
- J. Bouclé and N. Herlin-Boime, *Synth. Met.*, 2016, **222**, 3.
- J. Kim, S.-H. Lee, J. H. Lee and K. H. Hong, *J. Phys. Chem. Lett.*, 2014, **5**, 1312.
- J. Haruyama, K. Sodeyama, L. Han and Y. Tateyama, *J. Phys. Chem. Lett.*, 2014, **5**, 2903.
- J. Kang and L.-W. Wang, *J. Phys. Chem. Lett.*, 2017, **8**, 489.
- W.-J. Yin, T. Shi and Y. Yan, *Appl. Phys. Lett.*, 2014, **104**, 063903.
- M. H. Du, *J. Mater. Chem. A*, 2014, **2**, 9091.
- J. Kim, S.-H. Lee, J. H. Lee and K. H. Hong, *J. Phys. Chem. Lett.*, 2014, **5**, 1312.
- A. Buin, P. Pietsch, J. Xu, O. Voznyy, A. H. Ip, R. Comin and E. H. Sargent, *Nano Lett.*, 2014, **14**, 6281.
- W.-J. Yin, T. Shi and F. Yan, *J. Phys. Chem. C*, 2015, **119**, 5253.
- J. Kim, C.-H. Chung and K.-H. Hong, *Phys. Chem. Chem. Phys.*, 2016, **18**, 27143.
- M.-H. Du, *J. Phys. Chem. Lett.*, 2015, **6**, 1461.
- H. Uratani and K. Yamashita, *J. Phys. Chem. Lett.*, 2017, **8**, 742.
- L. Wei, W. Ma, C. Lian and S. Meng, *J. Phys. Chem. C*, 2017, **121**, 5905.
- K. Refson, P. R. Tulip and S. J. Clark, *Phys. Rev. B: Condens. Matter Mater. Phys.*, 2006, **73**, 155114.
- S. J. Clark, M. D. Segall, C. J. Pickard, P. J. Hasnip, M. J. Probert, K. Refson and M. C. Payne, *Z. Kristallogr.*, 2005, **220**, 567.
- J. P. Perdew, K. Burke and M. Ernzerhof, *Phys. Rev. Lett.*, 1996, **77**, 3865.
- A. Tkatchenko and M. Scheffler, *Phys. Rev. Lett.*, 2009, **102**, 073005.
- D. Vanderbilt, *Phys. Rev. B: Condens. Matter Mater. Phys.*, 1990, **41**, 7892.
- J. Lian, Q. Wang, Y. Yuan, Y. Shao and J. Huang, *J. Mater. Chem. A*, 2015, **3**, 9146.
- Y. Kawamura, H. Mashiyama and K. Hasebe, *J. Phys. Soc. Jpn.*, 2002, **71**, 1694.



- 54 C. C. Stoumpos, C. D. Malliakas and M. G. Kanatzidis, *Inorg. Chem.*, 2013, **52**, 9019.
- 55 G. Volonakis and F. Giustino, *J. Phys. Chem. Lett.*, 2015, **6**, 2496.
- 56 D. W. de Quilettes, S. M. Vorpahl, S. D. Stranks, H. Nagaoka, G. E. Eperon, M. E. Ziffer, H. J. Snaith and D. S. Ginger, *Science*, 2015, **348**, 683.
- 57 Q.-Q. Ge, J. Ding, J. Liu, J.-Y. Ma, Y.-X. Chen, X.-X. Gao, L.-J. Wan and J.-S. Hu, *J. Mater. Chem. A*, 2016, **4**, 13458.
- 58 W. Zhou, Y. Zhao, C. Shi, H. Huang, J. Wei, R. Fu, K. Liu, D. Yu and Q. Zhao, *J. Phys. Chem. C*, 2016, **120**, 4759.
- 59 J. Haruyama, K. Sodeyama, L. Han and Y. Tateyama, *Acc. Chem. Res.*, 2016, **49**, 554.
- 60 T. J. Jacobsson, J.-P. Correa-Baena, E. H. Anaraki, B. Philippe, S. D. Stranks, M. E. F. Bouduban, W. Tress, K. Schenk, J. Teuscher, J.-E. Moser, H. Rensmo and A. Hagfeldt, *J. Am. Chem. Soc.*, 2016, **138**, 10331.
- 61 J.-H. Im, I.-H. Jang, N. Pellet, M. Grätzel and N.-G. Park, *Nat. Nanotechnol.*, 2014, **9**, 927.
- 62 R. Lindblad, D. Bi, B.-w. Park, J. Oscarsson, M. Gorgoi, H. Siegbahn, M. Odelius, E. M. J. Johansson and H. Rensmo, *J. Phys. Chem. Lett.*, 2014, **5**, 648.
- 63 D.-Y. Son, J.-W. Lee, Y. J. Choi, I.-H. Jang, S. Lee, P. J. Yoo, H. Shin, N. Ahn, M. Choi, D. Kim and N.-G. Park, *Nat. Energy*, 2016, **1**, 16081.

